Evidence for magma entrapment below oceanic crust from deep seismic reflections in the western Somali basin

Daniel Sauter[1], Patrick Unternehr[2], Gianreto Manatschal[1], Julie Tugend[1], Mathilde Cannat[3], Patrick Le Quellec[2], Nick Kusznir[4], Marc Munschy[1], Sylvie Leroy[5], Jeanne Mercier de Lepinay[1], James W. Granath[6], and Brian W. Horn[7],

[1]*Institut de Physique du Globe de Strasbourg, CNRS UMR 7516, Université de Strasbourg, 1 rue Blessig 67084 Strasbourg cedex, France*

[2]*TOTAL- Exploration Production, place Jean Millier, La Défense 6, F-92078 Paris la Défense Cedex, France*

[3]*Institut de Physique du Globe de Paris, CNRS UMR 7154, Université Paris Diderot, 1, rue Jussieu 75238 Paris Cedex 05, France*

[4]*Department of Earth,Ocean & Ecological Sciences, University of Liverpool, Liverpool L69 3BX, UK*

[5]*UPMC ISTeP, CNRS UMR 7193, 4 place Jussieu, 75252 Paris Cedex 05, France*

[6]*ION E & P Consulting, 2306 Glenhaven Drive, Highlands Ranch, Colorado 80126, USA*

[7]*ION Geophysical, 2105 City West Boulevard, Houston, Texas 77042, USA*

TIMING OF THE EXTINCTION OF SPREADING AND LOCATION OF THE RIDGE AXIS

The West Gondwana (Africa) - East Gondwana (Seychelles, Madagascar, India, Antarctica, and Australia) plate kinematics, creating the Western Somali Basin (WSB), is still a matter of debate. Mesozoic magnetic anomalies have been identified in the WSB showing that the basement was formed by seafloor spreading in Jurassic time and ceased in Cretaceous time (Norton and Sclater, 1979; Ségoufin and Patriat, 1980). However, the identification of both the oldest and earliest isochrones is debated (Cochran, 1988; Coffin and Rabinowitz, 1987; Eagles and König, 2008; Rabinowitz et al., 1983; Ségoufin and Patriat, 1980).

The oldest magnetic anomalies identified in the West Somali Basins are M21-M22 (Cochran, 1988; Ségoufin et al., 2004; Ségoufin and Patriat, 1980), or M25 (Coffin and Rabinowitz, 1987; Eagles and König, 2008; Rabinowitz et al., 1983). Some authors have inferred Jurassic Quiet Zone crust between the oldest magnetic anomalies and the continental slope (Coffin and Rabinowitz, 1987) possibly as old as M41-40 (Gaina et al., 2013; Gaina et al., 2015). Spreading ceased either at M10 (Coffin and Rabinowitz, 1987; Eagles and König, 2008; Rabinowitz et al., 1983), M3 (Gaina et al., 2013; Gaina et al., 2015) or M0 (Cochran, 1988; Müller et al., 1997; Muller et al., 2008; Ségoufin et al., 2004; Ségoufin and Patriat, 1980; Seton et al., 2012) depending on the magnetic anomaly identification used.

One reason for the different interpretations is that the thick sediments in the WSB prevent direct observation of the extinct ridge axis and without a symmetry axis the identification of Mesozoic magnetic anomalies is more questionable. Therefore, we calculate the vertical gravity gradient (Rotstein et al., 2001) on the satellite-derived free air anomaly grid of Sandwell and Smith (2009) to locate the gravity low which is often observed over extinct slow spreading rate ridges (Downey et al., 2007). We also reinterpreted magnetic anomaly profiles, identifying the M0-M10 anomalies.

<u>Gravity data analysis:</u>
Between 43°E and 48°E, the axis defined by Ségoufin and Patriat (1980) and Cochran (1988) corresponds to a series of linear and well-marked negative gravity anomalies similar to those corresponding at the nearby extinct axis of the Mascarenes basin (Bernard and Munschy, 2000) (Fig. DR1). The observation that the relict ridge axis is the location of a free-air gravity anomaly low was already done by Cochran (1988) on gravity profiles. This contradicts Eagles and König (2008) who argued that the chronology of Ségoufin and Patriat (1980) is unsatisfactory because it has produced no axial gravity anomaly although the spreading rate determined by Ségoufin and Patriat (1980) was slow (<20km/Myr).

Except around 46°E, no gravity anomaly corresponds to the axis determined by Rabinowitz et al. (1983), Coffin and Rabinowitz (1987) and Eagles and König (2008), although the spreading rate

found by these authors was also slow (24-26 km/Myr). At 46°E, the gravity anomalies are clearly related with the Aldabra Island anomalies, a product of Cenozoic volcanism.

We conclude that between 43°E and 48°E, the fit between some well-marked linear negative gravity anomalies and Cochran's (1988) axis is good enough to locate the failed ridge axis with the gravity data.
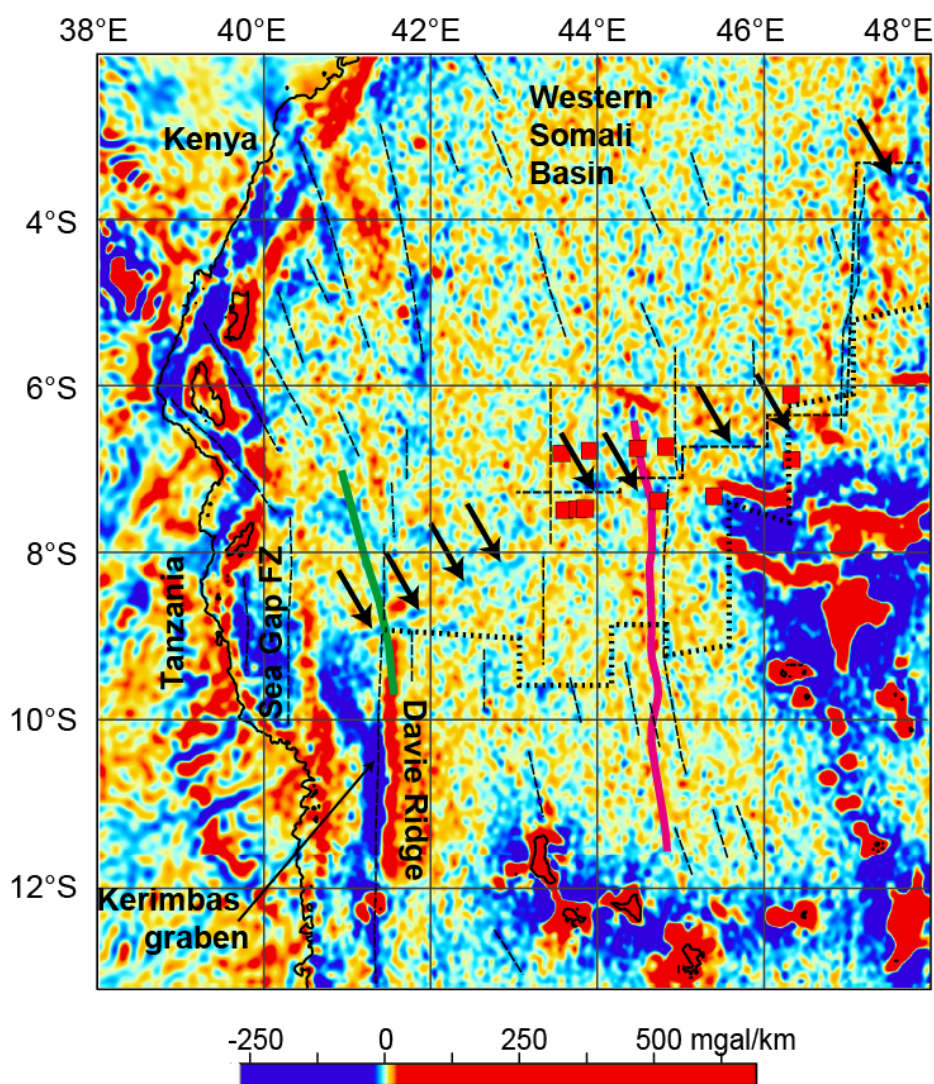

Figure DR1: Vertical gravity gradient calculated on the satellite-derived free air anomaly grid. Black arrows indicate the gravity anomaly inferred to show the extinct spreading axis. The thin black dashed line indicates the axis after (Cochran, 1988). The thick dotted line indicates the axis after (Rabinowitz et al., 1983). Thin black dashed lines show gravity lineations indicating spreading directions. Location of the seismic section is indicated by a thick green line. The thick magenta line indicate the location of the V3619d magnetic profile shown in fig. DR2.

To the west of 43°E we propose that the axis corresponds to a series of weaker and less linear gravity anomalies than between 43° and 48°E (Fig. DR1). Why the axis is less well marked in the gravity than to the east of 43°E is unclear. We suggest that the sediment cover which strongly increases toward the continent, helps to obscure the gravity signal of the extinct axis westward. Sediments are 3-3.5 km thick at 7°S 43°E, at the western end of the well-marked axis of Cochran (1988), and reach 5 km closer to the continent (Divins, 2006) and along the seismic section. The

age of the extinction, the spreading rate decrease or the magma budget may also have been different toward the continent. However the lack of magnetic data limits constraints on the kinematics in that area of the WSB (see next section).

Magnetic data analysis

We use all magnetic profiles available from the National Geophysical Data Center (NGDC) database (http://www.ngdc.noaa.gov/mgg) together with the French profiles of Ségoufin and Patriat (1980). The density of well-oriented magnetic profiles (the more or less NS trending ones) is very low in the WSB. There is no recent magnetic profile in that area. All profiles have been already used in previous studies by Ségoufin and Patriat (1980), Cochran (1988), Coffin and Rabinowitz (1987) or Rabinowitz et al. (1983).

Fig. DR2 shows our interpretation of magnetic profile V3619D which essentially agrees with that of Ségoufin and Patriat (1980) and Cochran (1988) and disagrees with that of Coffin and Rabinowitz (1987) and Rabinowitz et al. (1983). The axis determined from the gravity analysis is sited between M0y anomalies (126 Ma (Ogg, 2012)) which is the last identified anomaly before the Cretaceous magnetic quiet zone (Fig. 1, DR1-DR2). Assuming spreading in the WSB ceased shortly after M0 (at ~120 Ma following (Seton et al., 2012)), spreading rate was on average slow (28 km/Myrs) for the last 14 Myrs before extinction: the failed axis and anomaly M10y (~134 Ma (Ogg, 2012)) are spaced by ~200 km which gives a half-spreading rate of ~14 km/Myrs (200 km / 14 Myrs) (Fig. DR2).

However, the age of cessation of seafloor spreading in the WSB may be as young as late Aptian or even mid Albian. It is difficult to nail down the exact age of cessation because the sea-floor spreading probably slowly faded rather than stopped abruptly. Magnetic anomalies do not help to constrain this age because of the Cretaceous magnetic quiet zone. Moreover we cannot exclude that spreading have ceased earlier or later than M0 time in the western part of the WSB where no magnetic anomaly has been identified.

Our interpretation, with a cessation of spreading in the West Somali Basin shortly after M0, and not at M10 as suggested by Eagles and König (2008), agrees with the kinematic model of Seton et al. (2012). These authors note that the cessation of spreading at M10 results in the position of Africa relative to Madagascar and Antarctica that is incompatible with newly interpreted aeromagnetic data in the area (König and Jokat, 2010).
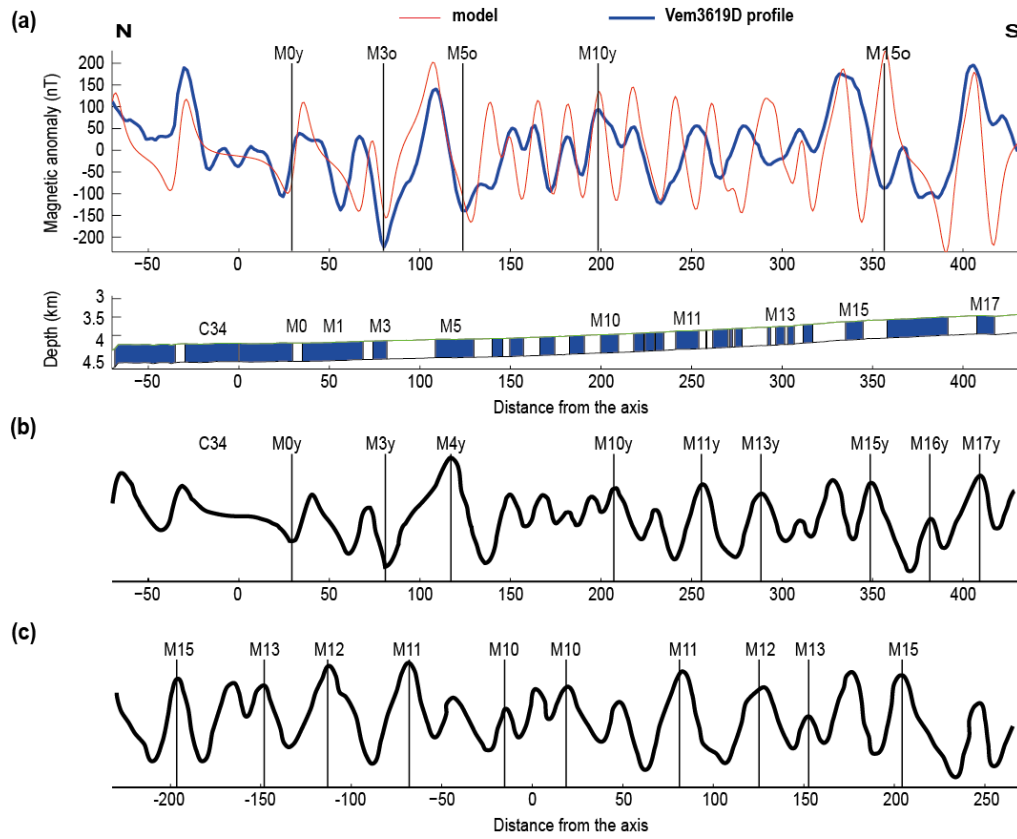
Figure DR2: Magnetic anomaly profile V3619D and corresponding forward models. (a) model proposed in this study, (b) model of Cochran (1988), (c) model of Rabinowitz et al., (1983). Note that both Cochran (1988) and Rabinowitz et al. (1983) used the time scale of Larson and Hilde (1975) with a different nomenclature for the M1-M5 sequence than in the more recent time scale of Ogg (2012): e.g. M3 corresponds to M3r and M4 corresponds to M5n in the Ogg (2012) time scale. See Fig. DR1 for the location of the profile. We compute model (a) using the MODMAG software (Mendel et al., 2005): we assume a 0.5 km thick source layer with a 5 A/m magnetization; the age at distance 0 km is assumed to be 120 Ma following (Seton et al., 2012); the mean half spreading rate is 18 km/Myrs between 120 Ma and 140 Ma (anomaly M15v); the effect of sloped polarity boundaries on magnetic anomaly amplitude has been modeled using the method of Tisseau and Patriat (1981) with a 0.7 contamination coefficient. Note that model (a) and (b) are very similar from the failed axis up to M10 anomaly. There are slight differences in the older part, from M10 to M15. Therefore we choose to retain a mean spreading rate of 14 km/Myrs obtained only between the axis and M10y magnetic anomaly.

SEISMIC DATA ACQUISITION AND PROCESSING

The seismic reflection section was acquired by ION Geophysical in December 2006. A single 9.3-km-long streamer of 124 active Syntrak 960 RDA sections, towed at a depth of 9.5 m, was used. Each 75 m section contained 3 active groups, each with a group length of 25 m. A total of 372 active channels were recorded on each shot point. Each channel received input from 32

Benthos hydrophones, each with a quoted sensitivity of 20 μV/μB. Compass and depth control units were used to maintain streamer depth control and to provide heading information for cable shaping. A single 6,008 cubic inch source, providing an output power of 156 bar m and peak-to-bubble ratio of 16.3, was towed at a depth of 8.5 m ± 1 m. This single source comprised 4 sub arrays with 40 Bolt Long Life sleeve guns, 10 per sub-array, ranging individually from 72 to 290 cubic inches. The sub-arrays were spaced every 8 m. Two depth transducers were fitted to each sub-array. Air pressure was maintained 2,000 psi ± 5% throughout the survey. The record length was 18,432 ms and the sample interval was 2 ms. The shot interval was 50 m and the vessel speed was 4.5 knots. Both the streamer and guns were positioned using GPS pods.

Pre-processing was a fairly typical workflow: after reformatting the SEG-D to ProMax, the data were resampled from 2 to 4 ms, the geometry was merged, and the result quality controlled. Gun and cable static corrections were applied, and corrections made for system delay. The data were converted to single phase, analysed for velocity, and a correction applied for spherical spreading. Noise attenuation was compensated, and channel amplitude corrected. Multiples were preliminarily handled at this stage with a free surface attenuation technique. At this point the line segments were merged and multiples treated with both high-resolution radon demultiple and apex-shifted demultiple routines. F-X deconvolution was applied as was a residual noise attenuation routine.

An initial Kirchhoff prestack time migration was performed using a smoothed model with RMS stacking velocities. Velocities were manually picked every 250 CDP to update the velocity model, and the migration was run again with the updated model. This procedure was iterated 3 times to get the velocities to converge, followed by an autopicker on every 2nd CDP to again update the model. This also was done three times to converge the velocities and ensure well-corrected gathers. This updated velocity model was run to produce the final prestack time migrated section, after which a residual move-out correction was applied.

DEPTH CONVERSION OF THE REFLECTORS

We used a simple velocity gradient to calculate the depth of the top basement reflector and of the R1, R2, R3 and R4 reflectors from the TWTT seismic section. We assume a 3 km/s velocity for the sediment layers between the seafloor and the top basement. A 6.5 km/s crustal velocity was then assumed for both U1 and U2 between the top basement and R2. Below R2 we assume an 8 km/s velocity for the mantle.

Units	Upper limit	Lower Limit	velocity
sediments	seafloor	top basement	3.0 km/s
U1 and U2	top basement	R2 reflector	6.5 km/s
mantle	R2 reflector		8.0 km/s

FIGURE DR3: DETAILED VIEWS OF THE SEISMIC PROFILE
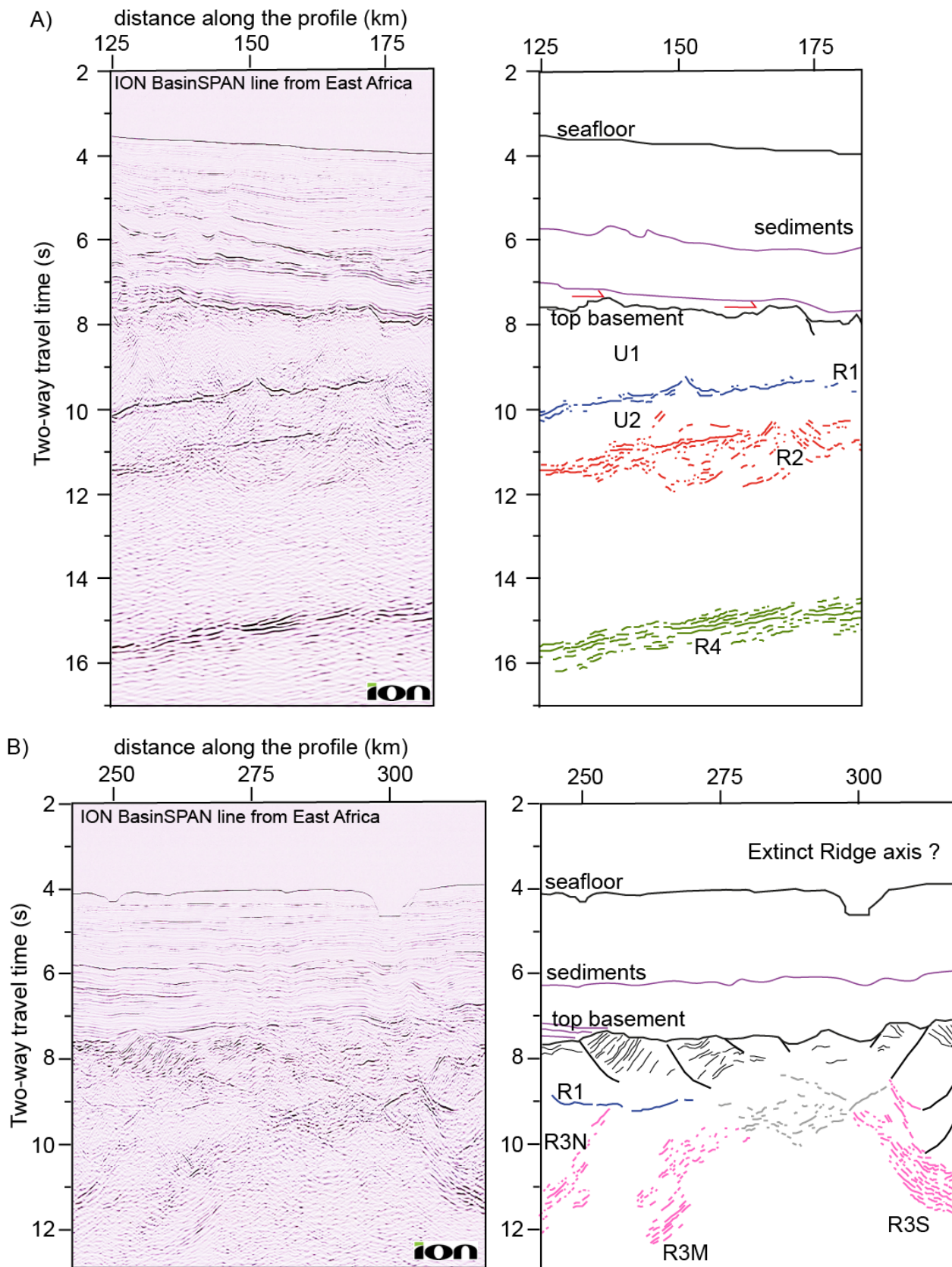
THERMAL MODELING

We explore here how the geometry of the R4 reflectors could be explained by a sloped isotherm becoming shallower toward the failed spreading axis. We used a simple half-space cooling model of the oceanic lithosphere (Turcotte and Schubert, 1982) (Figure 3). This type of model of conductive heat transfer cannot account for the thermal structure of the axial region of spreading ridges where the oceanic crust is strongly cooled by hydrothermal circulation (Stein and Stein, 1994). Convective cooling by hydrothermal circulation is especially vigorous at slow spreading ridges where the plate boundary corresponds to ~20 km wide axial deformation zone (Stein and Stein, 1994). We therefore do not intend to reproduce the thermal structure of the shallow axial part of the failed ridge but we restrain our approach to its deep off axis part. We keep the calculation as simple as possible and do not adjust parameters to obtain the best fit. We therefore disregard effect of ridge obliquity and assume a constant half-spreading of 15 km/Myrs (see the "Magnetic data analysis" section here above).

In order to explore the sensitivity of our model relative to the location of the ridge axis, we assume two possible locations for the spreading axis: at 270 and 290 km distance. In the latter case the axis is located at the center of the rift zone (i.e. at the midpoint between north-dipping and south-dipping basement faults) and coincides with the center of the negative gravity anomaly observed in the free air gravity map derived from satellite data (see Fig. DR1). However, our model does not account neither for the westward strongly decreasing magma budget, nor for the cooling of the lithosphere due to the cessation of spreading itself. Moreover, the rift zone between 250 and 300 km may correspond to a deformation zone along the Davie fracture zone. We therefore choose to shift the axis westward at 270 km distance (see Figure 3).

The obtained paleo ~1100°C isotherms, i.e. at the very base of the lithosphere, lie close to the reflector R4. The fit is better taking the axis at 270 km distance rather than at 290 km but, the two depth estimations for the ~1100°C isotherm are spaced by only ~3 km between 20 and 30 km depth below top basement. This depth difference is not significant considering our crude thermal modelling. Although rather persuasive (with a misfit < 6 km) both fits are approximate (Figure 3). We suggest that our assumptions about spreading rate, ridge obliquity, variation of magma budget during the extinction and the estimated depth of the R4 reflector may have led to these approximate fits.

GRAVITY INVERSION

Satellite-derived free-air gravity anomaly and bathymetry were used to determine mantle residual gravity anomaly, inverted in the three-dimensional spectral domain to determine Moho depth. Gravity inversion incorporates a thermal gravity anomaly correction and a parameterization of decompression melting to predict volcanic addition (Chappell and Kusznir, 2008b; Greenhalgh and Kusznir, 2007). Corrections for sedimentary thickness are

also included. The processing and sensitivity tests conducted on the parameters used for the gravity inversion are detailed hereafter.

The gravity inversion technique used to determine Moho depth, crustal thickness and lithosphere thinning distribution was carried out in the 3D spectral domain based on the scheme of Parker (1973). This method (described in detail in Greenhalgh and Kusznir (2007), Chappell and Kusznir (2008b), Alvey et al. (2008)), includes both a correction for lithosphere thermal gravity anomaly for continental and oceanic lithosphere and a parameterization of the decompression melting model of White and McKenzie (1989) to predict volcanic additions. A Butterworth low-pass filter with a cut-off wavelength of 100 km has been used to remove the short wavelength anomalies caused by shallow sources within the crust, hence unlikely to be due to Moho topography (Chappell and Kusznir, 2008b). We applied a constant velocity of 6.5 km.s^{-1} to the crustal basement (i.e. between the interpreted top basement and gravity inversed Moho) to convert Moho depth determined from gravity inversion into two-way travel time in order to enable the comparison with reflection seismic data.

Free-air gravity anomaly and bathymetry data used in the gravity inversion are from Sandwell and Smith (2009) and Smith et al. (2008). Sediment thickness data used in the gravity inversion to produce regional maps of crustal thickness (Fig. 1; Fig. DR4 and DR6) are taken from Divins (2006). Locally, to improve the resolution of the results, we also independently calculated the gravity inversed Moho along the profile (Fig. 2; Fig. DR5 and DR7) using sediment thickness from the corresponding depth-converted seismic line (ION BasinSPAN line). Tests show that the depth of Moho from the 3D gravity inversion determined for the seismic line is not sensitive to the method of extrapolating the observed sediment thickness observed on the seismic line outwards from the line (Kriging, nearest neighbour, triangulation). The gravity anomaly contribution from sediment thickness assumes a compaction-controlled density-depth relationship (Chappell and Kusznir, 2008a).

Among the parameters used in the gravity inversion technique, the reference Moho depth necessitates specific consideration and calibration (Cowie et al., 2015.) It can be calibrated against refraction seismic data on oceanic lithosphere (Chappell and Kusznir, 2008b; Cowie and Kusznir, 2012; Greenhalgh and Kusznir, 2007). The reference Moho depth used in the gravity inversion at the scale of the Western Somali basin is ~36 km (Fig. 1; Fig. DR4d). It was calibrated against refraction seismic data on oceanic lithosphere in the Western Somali basin (Coffin et al., 1986). The reference Moho depth strongly depends on deep mantle dynamic processes (Cowie and Kusznir, 2012; Cowie et al., 2015). The proximity of active hotpots to the south (e.g. Comores islands) seems to be responsible for dynamic uplift near the ION BasinSPAN line. The scattering of the points on the figure DR4d suggests that close to the sonobuoy 420 (Coffin et al., 1986) the reference Moho depth decreases reaching values close to ~34 km (Fig. DR4e). The strong influence of the reference Moho depth on Moho depth

variations is illustrated in figure DR5. Based on the calibration in figure DR4e, our preferred reference Moho depth for the gravity inversed Moho extracted along the profile is 34 km (Fig. 2; Fig. DR7). Reference Moho depth values of 36 and 32 km provide uppermost and lowermost boundaries for Moho depth in figure 2 (shaded area).
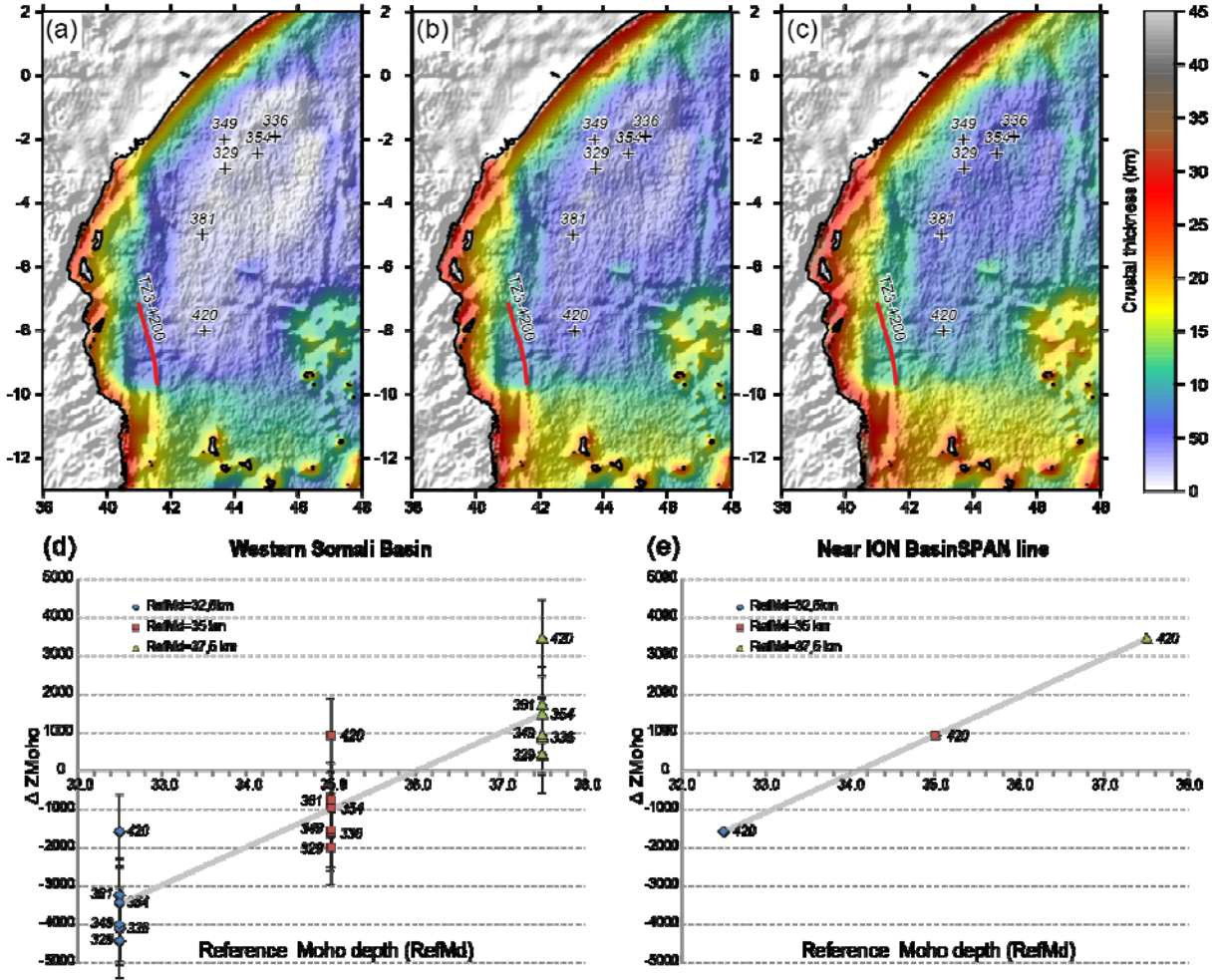

Figure DR4: Sensitivity to reference Moho depth. Sensitivity of crustal thickness predicted from gravity inversion for a reference Moho depth of (a) 32.5 km; (b) 35 km; and (c) 37.5 km. Crosses on crustal thickness maps indicate the location of seismic refraction Moho depth measurements (Coffin et al., 1986) used for reference Moho depth calibration. **Reference Moho depth calibration.** We plot the difference between gravity and seismic Moho depths, ΔZMoho, against reference Moho depth, ΔZMoho = Moho$_{GI}$ - Moho$_{Refraction}$. For each sonobuoy, the standard deviation was calculated. (d) At the scale of the Western Somali basin, the calibration gives a reference Moho depth ~ 36 km. (e) Reference Moho depth decreases to ~34 km close to the ION BasinSpan line.
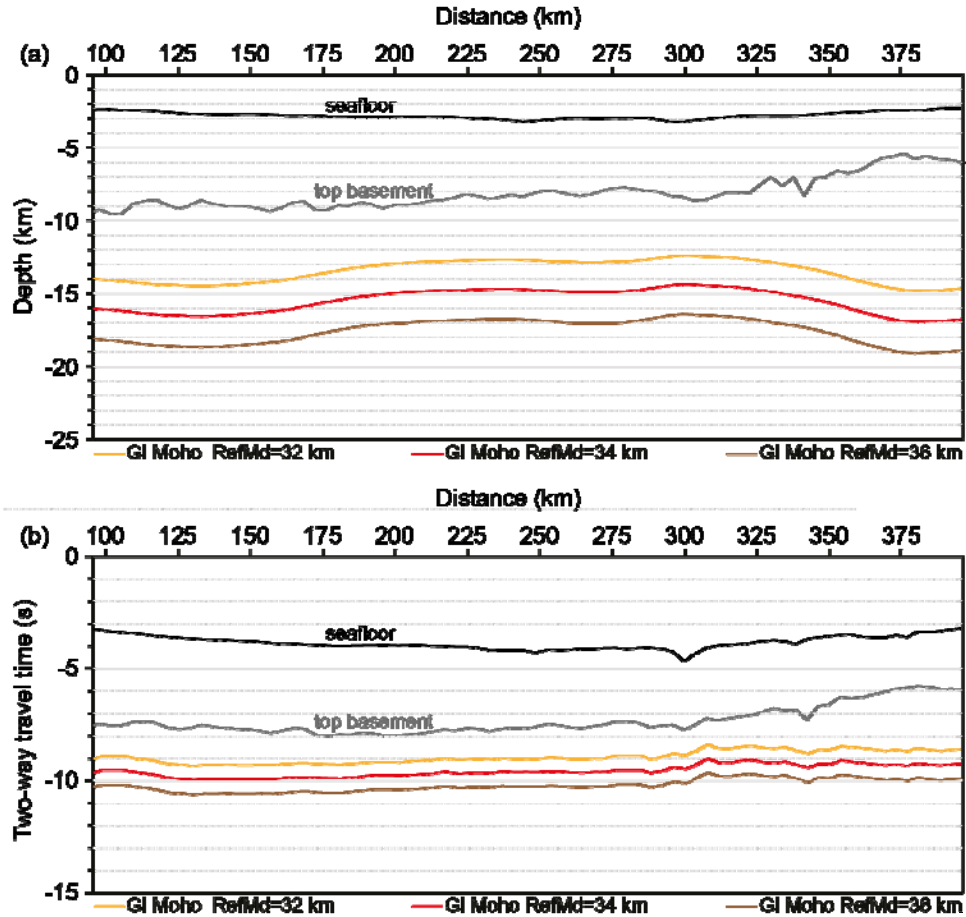
Figure DR5: Sensitivity to reference Moho depth. (a) Variations in depth of the gravity inversed Moho along the profile considering a reference Moho depth of 32, 34 and 36 km. (b) Same as (a) but for the time section.

In order to satisfy Smith's theorem (Smith, 1961), constant densities for the crust and mantle are used in the gravity inversion which is carried out in the wave-number domain (Chappell and Kusznir, 2008b). Mean densities for both continental and oceanic crusts are shown to be close to the 2850 kg/m^3 average used for gravity inversion (e.g.(Carlson and Herrick, 1990; Christensen and Mooney, 1995)). The density used for mantle rocks (3300 kg/m^3) is comparable with the range of densities suggested for mantle rock compositions (e.g.(Poudjom Djomani et al., 2001)). Considering identical average densities for oceanic and continental crust enables us to avoid inducing errors in the gravity inversion process by proposing a priori information on the distribution of oceanic and continental lithosphere. Using constant crustal densities of 2850 kg/m^3 also implies that our predicted Moho depth will tend to be shallower in areas of relatively lighter basement and deeper in areas of relatively denser crustal basement.

Stretching and thinning of continental lithosphere and oceanic sea-floor spreading results in elevated lithosphere geothermal gradients, lateral variations of temperature and density, and

consequently a lithosphere thermal gravity anomaly which must be included in the gravity inversion to determine Moho depth, crustal thickness and lithosphere thinning. The lithosphere thermal gravity anomaly correction is calculated using a 3D lithosphere thermal model. The initial syn-rift or syn-breakup lithosphere geotherm perturbation is defined using the lithosphere thinning factor (1-1/β) where β is the lithosphere stretching (McKenzie, 1978) and is determined from the gravity inversion. For continental margin lithosphere, breakup age is used to define cooling time to give the present day temperature structure and lithosphere thermal gravity anomaly correction; for oceanic lithosphere, the cooling time is obtained from ocean isochrones (taken from Müller et al. (1997)). The use of ocean isochrones to give lithosphere cooling times only (Fig. DR6a) rather than oceanic β = ∞ as well (Fig. DR6b) allows the gravity inversion to predict lithosphere thinning and oceanic and continental lithosphere distribution independently of a priori ocean isochrones information. We also tested a solution without using oceanic isochrones and assuming that the lithosphere thermal re-equilibration time is the same everywhere (Fig. DR6c). Almost no difference can be observed between the gravity inversed Moho without using ocean isochrones and that using ocean isochrones to give lithosphere cooling times only (Fig. DR7a).
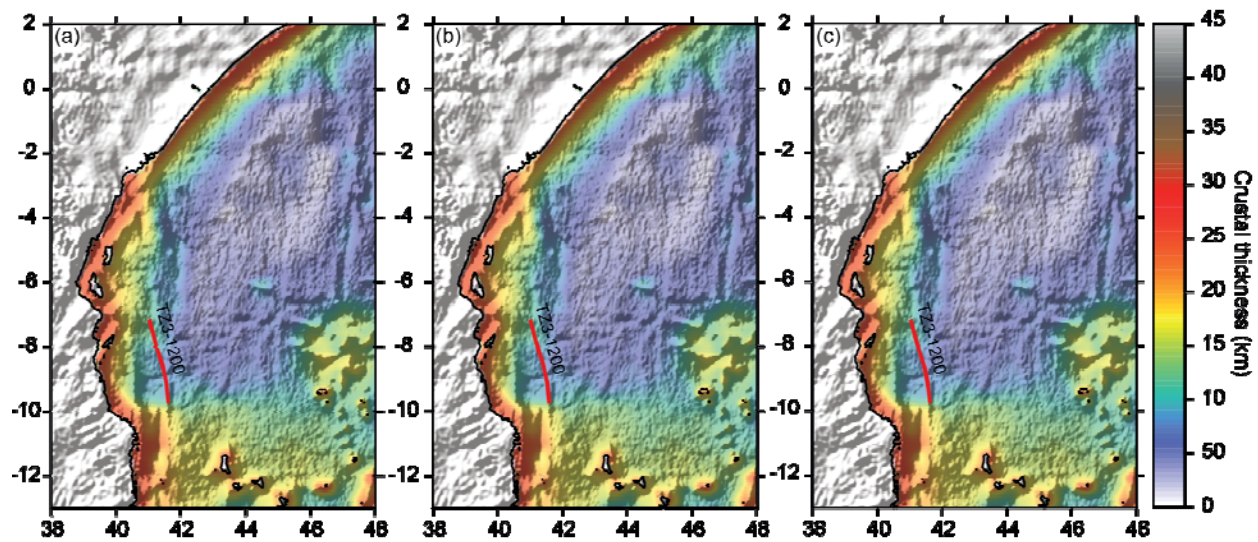

Figure DR6: Sensitivity of crustal thickness to the age of the lithosphere thermal perturbation used in the gravity inversion to calculate the lithosphere gravity anomaly correction. (a) Crustal thickness predicted from gravity inversion using oceanic isochrones to determine lithosphere thermal cooling time and a lithosphere thermal re-equilibration time of 165 Ma for regions with no oceanic isochrones. The magnitude of the lithosphere thermal perturbation is determined from the lithosphere thinning factor from gravity inversion for continental and oceanic areas. (b) As (a) but oceanic isochrones are used to give a lithosphere thinning factor of 1 to determine the lithosphere thermal perturbation. (c) Crustal thickness predicted without using oceanic isochrones and assuming a lithosphere thermal re-equilibration time of 125 Ma everywhere.

For the regional gravity inversion in the Western Somali basin (Fig. 1), a continental breakup age of 165 Ma is assumed. At the western termination of the fossil spreading system, the focus area of this study, oceanic isochrones are ill-defined and prone to substantial errors resulting in an unclear break-up age. We tested several break-up ages (110 Ma, 125 Ma and 165 Ma) to give the oceanic lithosphere thermal equilibration time and determine Moho depth (Fig. DR7). Changing the break-up age to a minimum value of 110 Ma or to a maximum value of 164 Ma, has a small effect on the gravity inversion compared to the influence of the reference Moho depth (Fig. DR4d). The gravity inversed Moho, extracted along the profile uses a break-up of 125 Ma within the range of values proposed (Fig. 2).
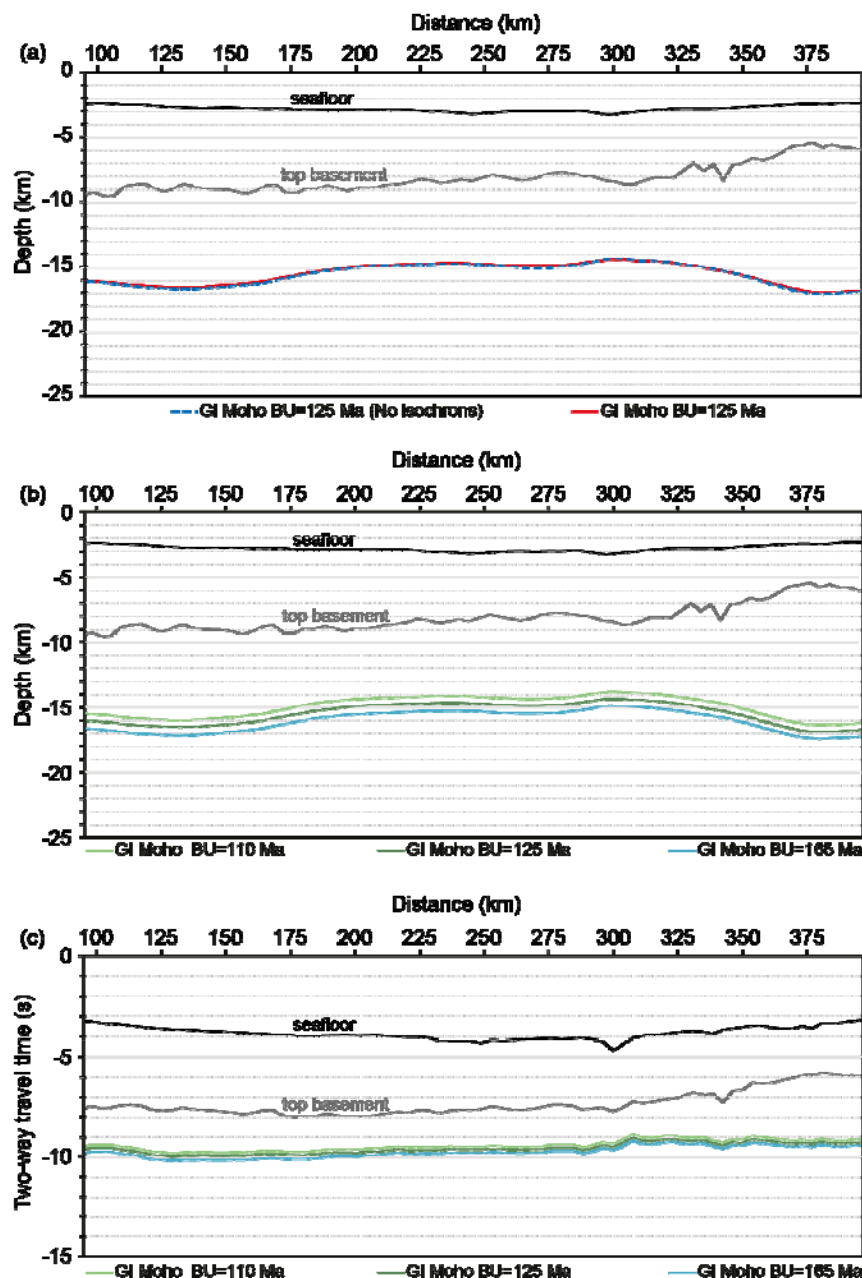

Figure DR7: (a) Sensitivity to the age of the lithosphere thermal perturbation used in the gravity inversion to calculate the lithosphere gravity anomaly correction. Comparison between Moho depth predicted from gravity inversion along the profile using oceanic isochrones to determine lithosphere thermal cooling time and a lithosphere thermal re-equilibration time of 125 Ma for regions with no oceanic isochrones (red curve) and Moho depth without using oceanic isochrones and assuming a lithosphere thermal re-equilibration time of 125 Ma everywhere (dashed blue curve). **(b)-(c) Sensitivity to break-up age.** (b) Variations in depth of the gravity inversed Moho along the profile considering a break-up age of 110 Ma, 125 Ma or 165 Ma. (c) Same as (b) but for the time section.

GRAVITY ANOMALY MODELLING

Figure DR8 shows that our gravity inversion model fits well the observed free air gravity data using the method described in Chappell & Kusznir (2008). There is a small misfit in the southern part across the inferred location of the failed axial valley and along the Davie Ridge. This may be partly explained by 3D effects. These effects are enhanced using a larger low-pass filter to smooth the data. Heterogeneities and lateral density variations in the crustal parts of the model may also explain the small misfits. This result corroborates the general crustal structure depicted from the interpretation of the seismic line.
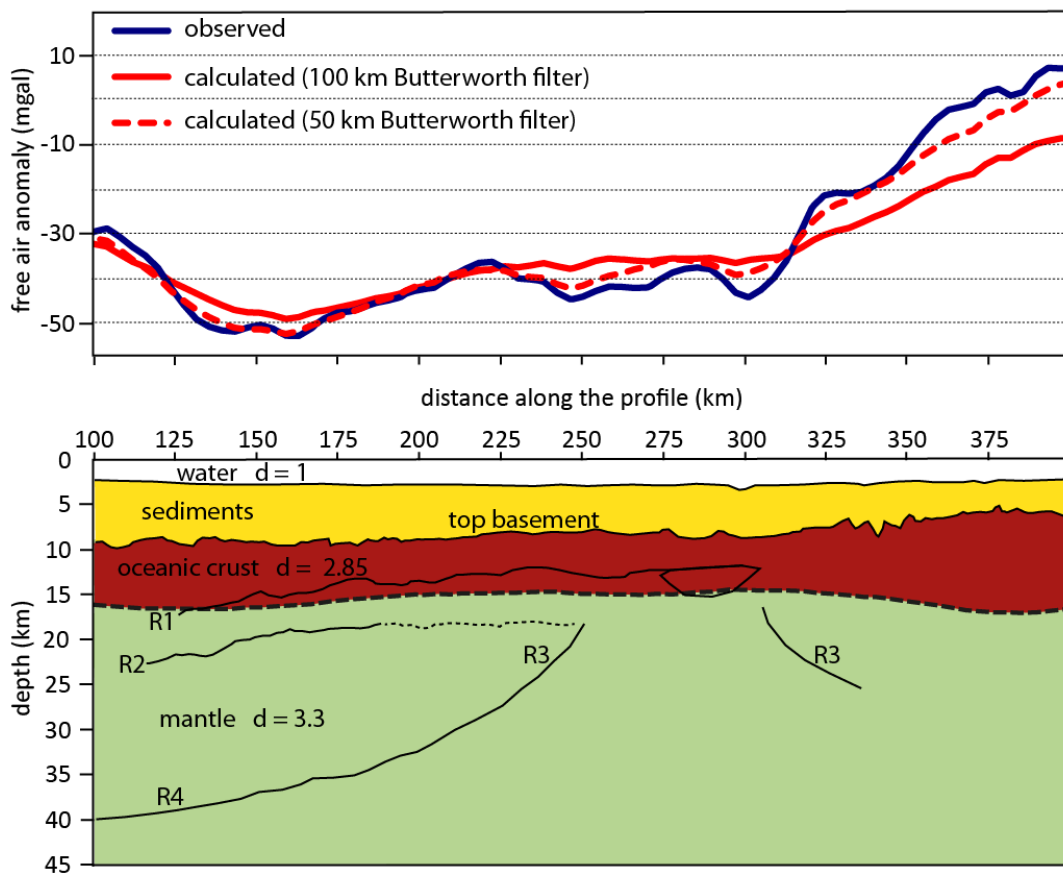

Fig DR8: **Gravity forward modeling along the seismic section**. The lower panel is the density model along the seismic line. The dashed line is the gravity inverted Moho (obtained using a Butterworth low-pass filter with a cut-off wavelength of 100 km). Density values are given in g/cm3. The crustal and mantle layers were modelled with homogeneous densities. For the sediments we use a compaction-controlled density-depth relationship (Chappell and Kusznir, 2008a). The top panel shows the measured gravity signal and the calculated ones using 2 Butterworth low-pass filters with cut-off wavelengths of 100 km and 50 km, respectively.

References

Alvey, A., Gaina, C., Kusznir, N.J., and Torsvik, T.H., 2008, Integrated crustal thickness mapping and plate reconstructions for the high Arctic: Earth and Planetary Science Letters, v. 274, p. 310-321.

Bernard, A., and Munschy, M., 2000, Le bassin des Mascareignes et le bassin de Laxmi (océan indien occidental) se sont-ils formés à l'axe d'un même centre d'expansion ?: Comptes Rendus de l' Académie des Sciences Série IIa:Sciences de la Terre et des Planètes, v. 330, p. 777-783.

Carlson, R.L., and Herrick, C.N., 1990, Densities and porosities in the oceanic crust and their variations with depth and age: Journal of Geophysical Research, v. 95, p. 9153-9170.

Chappell, A., and Kusznir, N., 2008a, An algorithm to calculate the gravity anomaly of sedimentary basins with exponential density-depth relationships: Geophysical Prospecting, v. 56, p. 249-258.

Chappell, A.R., and Kusznir, N.J., 2008b, Three-dimensional gravity inversion for Moho depth at rifted continental margins incorporating a lithosphere thermal gravity anomaly correction: Geophysical Journal International, v. 174, p. 1-13.

Christensen, N.I., and Mooney, W.D., 1995, Seismic velocity structure and composition of the continental crust: A global view: Journal of Geophysical Research: Solid Earth (1978–2012), v. 100, p. 9761-9788.

Cochran, J.R., 1988, Somali Basin, Chain Ridge, and origin of the Northern Somali Basin gravity and geoid low: Journal of Geophysical Research, v. 93, p. 11985-12008.

Coffin, M.F., and Rabinowitz, P.D., 1987, Reconstruction of Madagascar and Africa: Evidence From the Davie Fracture Zone and Western Somali Basin: Journal of Geophysical Research, v. 92, p. 9385-9406.

Coffin, M.F., Rabinowitz, P.D., and Houtz, R.E., 1986, Crustal structure in the Western Somali Basin: Geophysical Journal of the Royal astronomical Society, v. 86, p. 331-369.

Cowie, L., and Kusznir, N., 2012, Mapping crustal thickness and oceanic lithosphere distribution in the Eastern Mediterranean using gravity inversion: Petroleum Geoscience, v. 18, p. 373-380.

Cowie, L., Kusznir, N., and Manatschal, G., 2015, Determining the COB location along the Iberian margin and Galicia Bank from gravity anomaly inversion, residual depth anomaly and subsidence analysis: Geophysical Journal International, v. 203, p. 1355-1372.

Divins, D.L., 2006, Total-sediment-thickness database for the world's oceans and marginal seas, World Data Center for Geophysics & Marine Geology, Boulder, Colorado, USA.

Downey, N.J., Stock, J.M., Clayton, R.W., and Cande, S.C., 2007, History of the Cretaceous Osbourn spreading center: Journal of Geophysical Research B: Solid Earth, v. 112, p. B04102.

Eagles, G., and König, M., 2008, A model of plate kinematics in Gondwana breakup: Geophysical Journal International, v. 173, p. 703-717.

Gaina, C., Torsvik, T.H., van Hinsbergen, D.J.J., Medvedev, S., Werner, S.C., and Labails, C., 2013, The African Plate: A history of oceanic crust accretion and subduction since the Jurassic: Tectonophysics, v. 604, p. 4-25.

Gaina, C., van Hinsbergen, D.J.J., and Spakman, W., 2015, Tectonic interactions between India and Arabia since the Jurassic reconstructed from marine geophysics, ophiolite geology, and seismic tomography: Tectonics, v. 34, p. 875-906.

Greenhalgh, E.E., and Kusznir, N.J., 2007, Evidence for thin oceanic crust on the extinct Aegir Ridge, Norwegian Basin, NE Atlantic derived from satellite gravity inversion: Geophysical Research Letters, v. 34, p. L06305.

König, M., and Jokat, W., 2010, Advanced insights into magmatism and volcanism of the Mozambique Ridge and Mozambique Basin in the view of new potential field data: Geophysical Journal International, v. 180, p. 158-180.

Larson, R.L., and Hilde, T.W.C., 1975, A revised time scale of magnetic reversals for the Early Cretaceous and Late Jurassic: Journal of Geophysical Research, v. 80, p. 2586-2594.

McKenzie, D., 1978, Some remarks on the development of sedimentary basins: Earth and Planetary Science Letters, v. 40, p. 25-32.

Mendel, V., Munschy, M., and Sauter, D., 2005, MODMAG, a MATLAB program to model marine magnetic anomalies: Computers & Geosciences, v. 31, p. 589-597.

Minshull, T.A., 1996, Along-axis variations in oceanic crustal density and their contribution to gravity anomalies at slow-spreading ridges: Geophysical Research Letters, v. 23, p. 849-852.

Müller, R.D., Roest, W.R., Royer, J.-Y., Gahagan, L.M., and Sclater, J.G., 1997, Digital isochrons of the world's ocean floor: Journal of Geophysical Research, v. 102, p. 3211-3214.

Muller, R.D., Sdrolias, M., Gaina, C., and Roest, W.R., 2008, Age, spreading rates, and spreading asymmetry of the world's ocean crust: Geochemistry Geophysics Geosystems, v. 9.

Norton, I.O., and Sclater, J.G., 1979, A model for the evolution of the Indian Ocean and the breakup of Gondwanaland: Journal of Geophysical Research: Solid Earth, v. 84, p. 6803-6830.

Ogg, J.G., 2012, Geomagnetic polarity time scale *in* Gradstein, F.M., Ogg, J.G., Schmitz, M.D., and Ogg, G.M., eds., The Geological Time Scale 2012, Elsevier, p. 85-113.

Parker, R.L., 1973, The rapid calculation of potential anomalies: Geophysical Journal of the Royal astronomical Society, v. 31, p. 447-455.

Poudjom Djomani, Y.H., O'Reilly, S.Y., Griffin, W.L., and Morgan, P., 2001, The density of subcontinental lithosphere through time: Earth and Planetary Science Letters, v. 184, p. 605-621.

Rabinowitz, P.D., Coffin, M.F., and Falvey, D., 1983, The separation of Madagascar and Africa: Science, v. 220, p. 67-69.

Rotstein, Y., Munschy, M., and Bernard, A., 2001, The Kerguelen Province revisited: Additional constraints on the early development of the Southeast Indian Ocean: Marine Geophysical Researches, v. 22, p. 81-100.

Sandwell, D.T., and Smith, W.H.F., 2009, Global marine gravity from retracked Geosat and ERS-1 altimetry: Ridge segmentation versus spreading rate: Journal of Geophysical Research, v. 114, p. B01411.

Ségoufin, J., Munschy, M., Bouysse, P., and Mendel, V., 2004, Map of the Indian Ocean, CGMW (Commission for the Geological Map of the World).

Ségoufin, J., and Patriat, P., 1980, Existence d'anomalies mesozoiques dans le basin de Somalie. Implications pour les relations Afrique-Antarctique-Madagascar: Comptes Rendus de l' Académie des Sciences Série IIa:Sciences de la Terre et des Planètes, v. 291B, p. 85-88.

Seton, M., Müller, R.D., Zahirovic, S., Gaina, C., Torsvik, T., Shephard, G., Talsma, A., Gurnis, M., Turner, M., Maus, S., and Chandler, M., 2012, Global continental and ocean basin reconstructions since 200Ma: Earth-Science Reviews, v. 113, p. 212-270.

Smith, R.A., 1961, A uniqueness theorem concerning gravity fields: Proc. Cambridge Phil. Soc., v. 57, p. 865-870.

Smith, W., Sandwell, D., and Marks, K., 2008, New Global Bathymetry and Topography Model Grids, *in* AGU, ed., Fall Meeting Volume 1: San Fransisco, p. 0659.

Stein, C.A., and Stein, S., 1994, Constraints on hydrothermal heat flux through the oceanic lithosphere from global heat flow: Journal of Geophysical Research: Solid Earth, v. 99, p. 3081-3095.

Tisseau, J., and Patriat, P., 1981, Identification des anomalies magnétiques sur les dorsales à faible taux d'expansion: Méthode des taux fictifs: Earth and Planetary Science Letters, v. 52, p. 381-396.

Turcotte, D.L., and Schubert, D.L., 1982, Geodynamics: Applications of continuum physics to geological problems: New York, John Wiley & Sons, 450 p.

White, R., and McKenzie, D., 1989, Magmatism at rift zones: the generation of volcanic continental margins and flood basalts: Journal of Geophysical Research: Solid Earth (1978–2012), v. 94, p. 7685-7729.